

On the Enhanced Phosphorus Doping of Nanotextured Black Silicon

Giuseppe Scardera¹, Shaozhou Wang², Yu Zhang, Muhammad Umair Khan, Shuai Zou³, Daqi Zhang, Rasmus Schmidt Davidsen⁴, Ole Hansen, Ly Mai, David N. R. Payne, Bram Hoex⁵, and Malcolm D. Abbott

Abstract—The integration of nanotextured black silicon (B-Si) into solar cells is often complicated by its enhanced phosphorus doping effect, which is typically attributed to increased surface area. In this article, we show that B-Si's surface-to-volume ratio, or specific surface area (SSA), which is directly related to surface reactivity, is a better indicator of reduced sheet resistance. We investigate six B-Si conditions with varying dimensions based on two morphology types prepared using metal-catalyzed chemical etching and reactive-ion etching. We demonstrate that for a POCl_3 diffusion, B-Si sheet resistance decreases with increasing SSA, regardless of surface area. 2-D dopant contrast imaging of different textures with similar surface areas also indicates that the extent of doping is enhanced with increasing SSA. 3-D diffusion simulations of nanocones show that both the extent of radial doping within a texture feature and the metallurgical junction depth in the underlying substrate increase with increasing SSA. We suggest SSA should be considered more readily when studying B-Si and its integration into solar cells.

Index Terms—Black silicon, phosphorus doping, silicon nanotexture, surface area, surface-to-volume ratio.

I. INTRODUCTION

NANOTEXTURED silicon often falls under the collective label of black silicon (B-Si) which typically describes surfaces with low reflectance across a wide wavelength range (ultraviolet to near-infrared) and which appear black to the eye. B-Si can be prepared using a myriad of techniques and covers a wide range of surface morphologies and feature dimensions (from nano to micron-scale), including nanoporous layers [1],

[2], microstructures with tapered conical spikes [3]–[5], high aspect ratio nanoscale needles, vertical pores, or columns [6], inverted submicron structures [7]–[9], and highly ordered arrays of nanorods, cones [10], and pencils [10]–[12], as well as micropillars and micropencils [13]. B-Si nanotextures are of particular interest for photovoltaic applications because of their low reflectance and enhanced optical absorption, which could enable higher solar cell efficiencies. B-Si texturing processing incorporating metal-assisted chemical etching (MACE) or metal-catalyzed chemical etch (MCCE) with subsequent alkaline or acidic etching have already been adopted for industrial multicrystalline solar cells [9], [14]. However, there are challenges with integrating B-Si into solar cells including increased surface recombination associated with its increased surface area and the increased Auger recombination associated with its enhanced doping effect [15]. Studies of doped B-Si typically focus on recombination mitigation strategies, including additional texture modifications [15]–[17], advanced passivation techniques [18]–[20], modified diffusion processes [18], [21] or a transition to larger micron-scale features [13]. As such, only cursory explanations of the enhanced doping are typically provided. We believe that researchers studying B-Si recombination losses, for example, would benefit from a better understanding of its enhanced doping effect.

When subjected to the same phosphorus diffusion process silicon wafers with B-Si surfaces often exhibit a lower sheet resistance compared to a reference planar surface. This enhanced doping effect has been reported for multiple B-Si texturing techniques subjected to POCl_3 diffusion, including MACE [15]–[17], reactive-ion etching (RIE) [22], [23], plasma immersion ion implantation [24], and plasma-less atmospheric pressure dry etching [25]. Enhanced doping with POCl_3 has also been previously observed for more nanoporous structures including stain etched porous silicon [26] and deposited silicon nanoparticle layers [27]. It should be noted that enhanced phosphorus doping has also been reported for nanopencil [11] and micropencil [13] textures employing spin-on-dopants with subsequent annealing.

Multiple studies have indicated that for high aspect ratio black silicon features, the phosphorus doping can occur radially from all directions thus leading to enhanced doping [15]–[17], [22], [24], [28]. The full radial doping of nanoscale unit texture features has been reported for 2-D and 3-D diffusion simulations [22], [25]. Deeper junction formation from the tip of an upright nanotexture feature compared to the edge of its base (i.e., valleys between features) has been observed using electron

Manuscript received October 14, 2020; revised December 15, 2020; accepted December 22, 2020. Date of publication January 20, 2021; date of current version February 19, 2021. This work was supported in part by the Australian Government via the ARENA 2017/RND009 project. (Corresponding author: Malcolm D. Abbott.)

Giuseppe Scardera, Shaozhou Wang, Yu Zhang, Muhammad Umair Khan, Ly Mai, Bram Hoex, and Malcolm D. Abbott are with the University of New South Wales, Sydney, NSW 2052, Australia (e-mail: g.scardera@unsw.edu.au; shaozhou.wang@unsw.edu.au; yu.zhang@unsw.edu.au; m.umair@unsw.edu.au; ly.mai@unsw.edu.au; b.hoex@unsw.edu.au; m.abbott@unsw.edu.au).

Shuai Zou and Daqi Zhang are with the Canadian Solar Inc., Jiangsu 180000, China (e-mail: shuai.zou@canadiansolar.com; daqi.zhang@canadiansolar.com).

Rasmus Schmidt Davidsen and Ole Hansen are with the Technical University of Denmark, 101A, Lyngby, Denmark (e-mail: rasda@dtu.dk; ohan@dtu.dk).

David N. R. Payne is with the University of New South Wales, Sydney, NSW 2052, Australia, and also with the Macquarie University, Sydney, NSW 2052, Australia (e-mail: david.payne@mq.edu.au).

Color versions of one or more of the figures in this article are available online at <https://doi.org/10.1109/JPHOTOV.2020.3047420>.

Digital Object Identifier 10.1109/JPHOTOV.2020.3047420

beam induced current measurements [25], [28] and 2-D dopant contrast imaging [18].

B-Si enhanced phosphorus doping is typically attributed to its increased surface area and more specifically to its surface-area-to-projected-area ratio or enhanced area factor (EAF) [15]–[17], [22], [24], [25], [28]. The clearest (and most statistically significant) trend between B-Si texture variation and sheet resistance was reported by Kafle *et al.* [25], however those results were presented in terms of etched thickness and not explicitly in terms of surface area. Zhong *et al.* reported sheet resistance variation with measured texture surface area, but both parameters spanned a very limited range [24]. It has also been suggested that increasing the EAF of high aspect ratio B-Si features would further enhance radial doping [17], but limited data is available to demonstrate this effect and detailed simulation studies of varying unit dimensions (and surface area) have not been reported.

In this article, we investigate two types of B-Si morphology (MCCE and RIE) which together span a wide range of surface features. We use atomic force microscopy (AFM) to measure both EAF and SSA. We subject these textures to a POCl_3 diffusion process and study the role of EAF and SSA in the enhanced doping behavior of B-Si by means of sheet resistance measurements, 2-D dopant contrast imaging, and 3-D diffusion simulations.

II. SURFACE REACTIVITY AND ENHANCED DOPING

A. Specific Surface Area (SSA) and Surface Reactivity

As a silicon nanofeature decreases in size, its surface-to-volume ratio (i.e., SSA) increases. As a result, the fraction of surface atoms (i.e., ratio of surface atoms to internal atoms within its volume) increases, which yields an increase in surface energy which, in turn, leads to altered bulk properties, like the lower melting point of silicon nanoparticles [29] and the increase in initial oxidation rates for silicon nanoparticles [30] and silicon nanowires [31].

In order to extend the concept of SSA to B-Si, we consider the simplified case of an ideal silicon pyramid texture with varying dimensions, along with a reference planar surface, and calculate the corresponding fraction of silicon surface atoms and SSA, as shown in Fig. 1. We assume the pyramids comprise of a $\langle 100 \rangle$ base and $\langle 111 \rangle$ lateral faces, with a 54.74° inclination angle (i.e., the angle between those two crystallographic planes). We use the $\langle 111 \rangle$ plane density of $7.83 \times 10^{14} \text{ cm}^{-2}$ and silicon density of $5 \times 10^{22} \text{ cm}^{-3}$ to calculate the fraction of silicon atoms from the pyramid lateral surface area and volume. The pyramid base dimensions are varied from 2.5 nm (largest SSA) to $100 \mu\text{m}$ (smallest SSA). By keeping the inclination angle fixed and varying the dimensions of the pyramid, we can calculate various SSA values for a fixed EAF value of ~ 1.7 . For the reference planar, silicon surface we assume a $\langle 100 \rangle$ orientation with a plane density of $6.78 \times 10^{14} \text{ cm}^{-2}$. As the planar surface has no texture (and thus no texture volume), we use the volume of the projected underlying substrate, which includes the entire substrate thickness, assumed here to be $180 \mu\text{m}$, when calculating SSA, thus giving a value approaching zero. Fig. 1 highlights that as the unit texture feature becomes

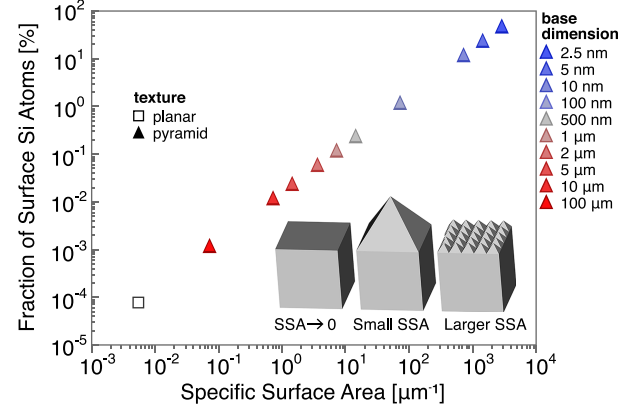
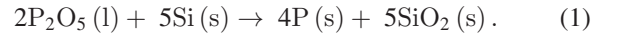


Fig. 1. Fraction of Si surface atoms versus SSA calculated for ideal pyramids ($\langle 100 \rangle$ base and $\langle 111 \rangle$ faces), and for a reference planar surface. Pyramid base dimensions vary from 2.5 nm (largest SSA) to $100 \mu\text{m}$ (smallest SSA) while maintaining a fixed EAF (~ 1.7). Inset: schematics for planar and pyramid textures.

smaller, SSA increases with a corresponding increase in fraction of silicon surface atoms, which in turn indicates increasing surface reactivity, despite all pyramid conditions having the same EAF.

B. Enhanced Phosphorus Doping

The phosphorus doping of silicon from a deposited dopant source (via POCl_3 , phosphorus-containing spin-on-dopants, or phosphoric acid sprays [32]) is driven by a surface reaction. Specifically, a coating of P_2O_5 reacts with surface silicon atoms to create free phosphorus atoms which diffuse into the underlying silicon via the following surface reaction:



The simultaneous growth of P_2O_5 and SiO_2 on the wafer surface results in a thin film typically referred to as phosphosilicate glass (PSG). Furthermore, the diffusion of phosphorus atoms into the silicon is driven by the phosphorus concentration gradient established between the surface and the underlying silicon substrate, as described by the general diffusion equation

$$\frac{\partial C_P}{\partial t} = \nabla \cdot (D_P \nabla C_P) \quad (2)$$

where C_P is the phosphorus concentration per unit volume, and D_P is the diffusivity of phosphorus in silicon, which is also a function of C_P [32] and thus indirectly of depth. This equation is typically simplified to a 1-D case for planar surfaces, but B-Si textures can be viewed as a collection of 3-D features in intimate contact with the underlying substrate.

We suggest the extent of a texture's doping via (1) will depend on its surface reactivity (and thus SSA) and not merely on the silicon surface area available for the reaction, as is commonly assumed. A more reactive surface will enhance the extent of radial doping within the texture feature. Features with sufficiently high SSA will be fully n^+ doped throughout their volume. This enhanced local doping may also establish a larger phosphorus concentration gradient between the feature and the underlying

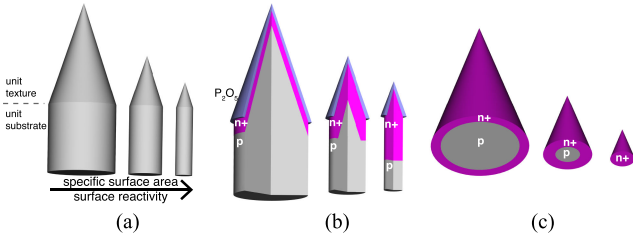


Fig. 2. Schematics highlighting proposed texture doping behavior. (a) Conical unit textures (and underlying substrate) with decreasing unit texture volume. (b) Corresponding post-diffusion cross-sections with P_2O_5 coating and extent of n^+ doping indicated. (c) Corresponding doped texture features with bottom views indicating the progression of radial doping.

substrate, leading to deeper junction formation via (2). The proposed impact of enhanced surface reactivity associated with increasing texture SSA on doping is illustrated in Fig. 2.

III. EXPERIMENT AND SIMULATION DETAILS

A. B-Si Fabrication

MCCE black silicon textures were applied to 180 μm thick, 156×156 mm pseudo-square, 2.68 $\Omega\text{-cm}$, p-type monocrystalline Cz silicon wafers. Reference chemically polished planar and random pyramid texture conditions were also prepared on Cz wafers. The MCCE process was preceded by a damage removal step. Wafers were then dipped in an AgNO_3 solution, which created nanopits, and subsequently dipped in an HF-HNO_3 solution, which converted the nanopits into inverted texture features. Different MCCE texture conditions (MCCE-1 to MCCE-3) were achieved by varying the post-nanopitting etch time, with MCCE-1 corresponding to the longest etch time and MCCE-3 to the shortest. More processing details are available in [9].

RIE B-Si textures were prepared with a noncryogenic RIE process using a SPTS Pegasus system with a temperature of -20°C , SF_6 and O_2 plasma with a 7:10 gas flow ratio, a total chamber pressure of 38 mTorr, 3000 W coil power, and 10 W platen power. The RIE textures were prepared as two sets of 350 μm thick, round, double-side polished, Cz p-type (100) silicon wafers. In the first set, RIE texture was applied to 4-inch wafers. Different RIE texture conditions (RIE-1, -2, -3) were achieved by varying the process time (2, 8, and 16 min, respectively). The 4-inch wafers were used for optical and structural characterization. The same process conditions were applied to the second set of 6-inch wafers for subsequent phosphorus diffusion testing.

B. Texture Characterization

Reflectance spectra were measured using a Perkin Elmer 1050 spectrophotometer equipped with an integrating sphere. The weighted average reflectance (WAR), which is the average reflectance weighted by the number of available photons from a standard AM1.5 solar spectrum, was calculated between 350 and 1120 nm following [33]. Scanning electron microscope (SEM) images were obtained using a field-emission FEI NanoSEM 450 using a 5 kV beam accelerating voltage and a 5.0 mm working distance.

EAFs and SSAs were determined by means of AFM. The AFM scans were measured with a Bruker ICON in tapping-mode employing a TESP diamond-like carbon-coated silicon probe with a nominal tip radius of 18 nm. Scan areas were either 20 by 20 μm using 768 line-scans or 10 by 10 μm using 512 line-scans. Surface areas and texture layer volumes were determined using the Gwyddion software [34]. The surface areas were calculated using a triangulation method and the texture volumes were calculated from the integral of the surface heights across the scan areas [30]. Prior to calculating surface areas and volumes, the AFM raw data were processed with a mean plane leveling algorithm and the height minima values were shifted to zero.

It should be noted that the volume calculation from AFM scans is very sensitive to the background signal and background subtraction methods. In order to minimize substrate background “waviness,” often observed for diamond wire sawn silicon wafers [35], a chemical polishing step was employed prior to creating the MCCE B-Si textures. For RIE samples, wafers with a “mirror-finish” polish were used. Also, the same plane leveling background subtraction was used for all conditions for consistency. The texture volume calculation is also sensitive to measurement artefacts which create outliers in the data. Therefore, AFM scans were cross-checked with SEM imaging to ensure that such errors were avoided. It should be noted that greater care was required for the MCCE scans which were more prone to artefacts, due to protruding and overhanging features along feature edges. SEM cross-checking was also employed to ensure that AFM scans were detecting smaller features, particularly for the RIE conditions.

C. B-Si Phosphorus Doping

POCl_3 diffusion was performed with a Tempress TS81254 quartz tube diffusion furnace. The diffusion process consisted of a 25-min POCl_3 deposition step at 775°C , with a $\text{POCl}_3:\text{O}_2$ ratio of 600:600 sccm and background N_2 flow of 7.5 slm, followed by a 25-min drive-in step at 865°C in N_2 ambient. Sheet resistance was measured using a Sunlab Sherrescan four-point probe. Pseudo-square samples were measured at 49 equidistant points across the wafer, while the smaller round wafers were measured at 21 equidistant points across the wafer avoiding a region of nonuniformity along the edges.

2-D doping distribution was characterized with SEM dopant contrast imaging (SEMDCI), where p-type regions exhibit bright contrast and n-type regions exhibit darker contrast [36], [37]. Cross-sectional SEMDCI images were obtained with the FEI NanoSEM 450 using a 1 kV beam accelerating voltage and a 2.5 mm working distance. Samples were freshly cleaved just prior to placing them into the SEM vacuum chamber. The phosphorus profile for the planar reference was measured via time-of-flight secondary ion mass spectroscopy (ToF-SIMS) using an ION-TOF TOF SIMS⁵.

D. B-Si Phosphorus Diffusion Simulations

The 3-D numerical simulations were performed with the Sentaurus Process simulator [38]. A cuboid unit substrate with a 180 μm thickness and a $5.27 \times 10^{15} \text{ cm}^{-3}$ boron base doping was employed. Two nanocone surface features (on cuboid

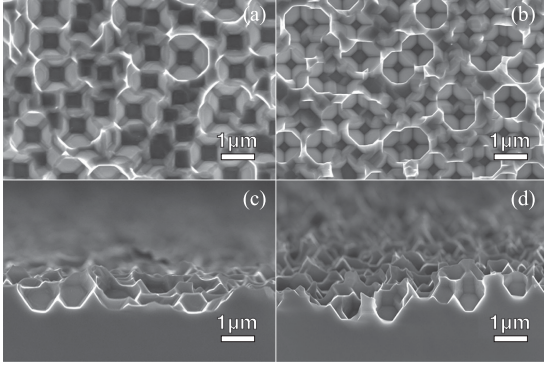


Fig. 3. Plan-view SEM images for MCCE conditions with the (a) longest post-nanopitting etch time (MCCE-1) and (b) the shortest post-nanopitting etch time (MCCE-3) and their corresponding cross-sectional images, (c) and (d), shown directly below them.

unit substrates) with different EAF and SSA values were also simulated. The simulated diffusion process was the same as the experimental process described above. The phosphorous diffusion was modeled by the charged-pair diffusion model, following (2) [38], with various diffusivities governed by the Arrhenius law. The various diffusivity parameters were taken from [38] or determined from fitting the ToF-SIMS data for the planar condition, as indicated below. The model employed: first, diffusion via PV^{2-} in the heavily doped region with a prefactor of 3.2×10^{-3} (fitting) and an activation energy of 3.5 eV (fitting); second, diffusion via PI^{-} in the lightly doped region with a prefactor of 1 [38] and an activation energy of 3.647 eV [38]; and third, diffusion via PI in the lightly doped region with a prefactor of 0.9 (fitting) and an activation energy 3.482 eV [38]. It was assumed that the PSG thickness was 40 nm and the initial phosphorous concentration in the PSG was $2 \times 10^{22} \text{ cm}^{-3}$, which were process-dependent fitting parameters. The PSG-Si segregation coefficient was assumed to be 6 [38] and a simple solid solubility model for phosphorous activation was used, employing a pre-factor of 1.85×10^{22} [38] and an activation energy of 0.27 eV [38].

IV. RESULTS AND DISCUSSION

A. B-Si Morphology

The plan-view SEM images for the MCCE conditions with the longest and shortest post-nanopitting etch times are shown in Fig. 3(a) and (b), respectively. The MCCE B-Si textures exhibit inverted-frustum-pyramid-like features. Fig. 3(a) and (b) indicates a clear change in the lower square base size and the diameter of the feature opening with each time. The corresponding cross-sectional SEM images, shown in Fig. 3(c) and (d), indicate a subtle change in feature depth, but less pronounced overhanging features for the longer post-nano-pitting etch.

The plan-view SEM images for the RIE B-Si conditions with the shortest and longest etch times are shown in Fig. 4(a) and (b), respectively. These images indicate a significant change in feature base size. The corresponding cross-sectional SEM images, shown in Fig. 4(c) and (d), show that the RIE B-Si

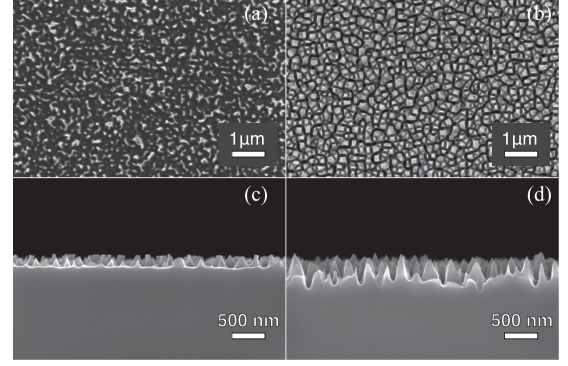


Fig. 4. Plan-view SEM images for RIE conditions with the (a) shortest etch time (RIE-1) and (b) the longest etch time (RIE-3) and their corresponding cross-sectional images, (c) and (d), shown directly below them.

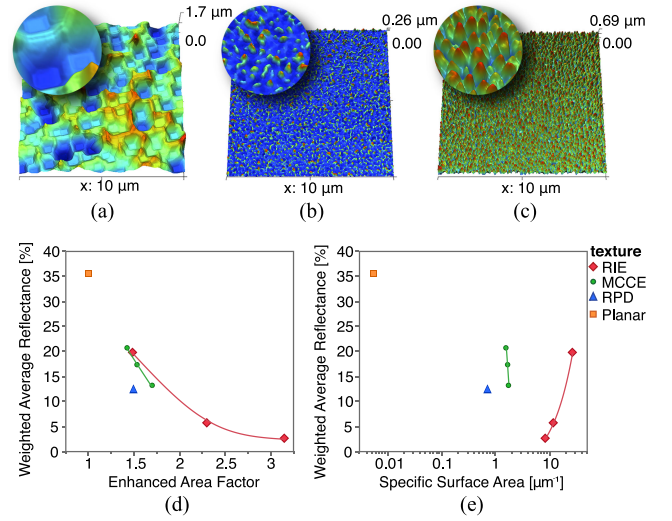


Fig. 5. AFM scans (same height scale) for (a) the longest post-nanopitting etch time MCCE condition (MCCE-1), (b) the shortest etch time RIE condition (RIE-1), and (c) the longest etch time RIE condition (RIE-3). Zoom-in insets presented to highlight texture features. (d) WAR versus EAF and (e) WAR versus SSA for all conditions.

textures exhibit upright conical features and also indicate a significant increase in feature height with longer etch time. We can qualitatively see in Fig. 4 that RIE-3 exhibits higher surface area and larger volume unit features compared to RIE-1. We are therefore able to qualitatively conclude from the SEM measurements that RIE-1 has a lower EAF, but higher SSA than RIE-3.

Fig. 5(a)–(c) shows the AFM scans, on the same height scale, for the longest post-nanopitting etch time MCCE condition and for the shortest and longest RIE process conditions, respectively. Good qualitative agreement is observed between SEM imaging and AFM scans.

The WAR vs. EAF (extracted from AFM) for all the texture conditions are shown in Fig. 5(d). The MCCE conditions exhibit decreasing WAR with decreasing post-nanopitting etch time. The RIE B-Si conditions exhibit decreasing WAR with increasing RIE process time. The WAR for both the MCCE and RIE conditions decreases with increasing EAF values. However,

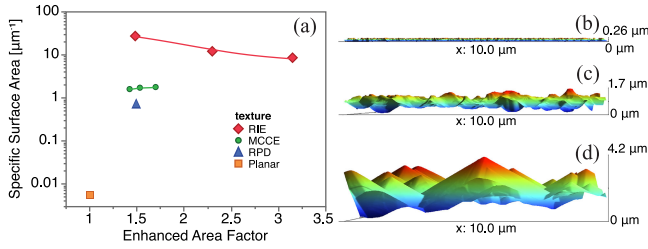


Fig. 6. (a) SSA versus EAF for various textured silicon samples and side-views of AFM scans presented on the same height scale for (b) B-Si RIE-1, (c) B-Si MCCE-2, and (d) RPD, which all have similar EAF values of ~ 1.5 .

the WAR vs. SSA trends are very different for the two B-Si morphology types, as shown in Fig. 5(e). For MCCE the WAR decreases with increasing SSA, whereas for RIE the WAR decreases with decreasing SSA.

A more effective way of comparing the different morphologies is by plotting SSA vs. EAF, as shown in Fig. 6(a). For the MCCE conditions, the SSA values increase with increasing EAF (corresponding to decreasing post-nanopitting etch times). However, given the small range of texture variation within that set, only marginal changes for both parameters were extracted for MCCE. It should be noted that we found the volume calculation to be more sensitive than the surface area calculation to artefacts associated with overhanging features. Therefore, we believe that MCCE conditions have higher SSA measurement uncertainty. As the extent of overhangs increase with decreasing post-nanopitting etch time, we also believe that such uncertainties increase from MCCE-1 to MCCE-3. For the RIE conditions, the SSA values decrease with increasing EAF (corresponding to increasing etch time). For the planar reference condition, the EAF is very close to 1 as expected given the nominally flat surface, while the SSA approaches zero (using the approach in Section II-A). Three conditions in Fig. 6(a) have very similar EAF values of ~ 1.5 , but different SSA values (RPD, MCCE-2, and RIE-1). The varying texture volume for these conditions is apparent from the side-view AFM scans shown in Fig. 6(b)–(d).

B. B-Si Phosphorus Doping

A variability plot of post-diffusion (and post-PSG-removal) sheet resistance for all conditions is shown in Fig. 7(a) with corresponding SSA and EAF values indicated. The changes in sheet resistance are marginal across the MCCE conditions, which is consistent with the small changes in their corresponding SSA values. The sheet resistance change between MCCE-2 and MCCE-3 appears large for the small change in SSA, but we attribute this to the increased SSA measurement uncertainty mentioned above. The RIE conditions exhibit a larger change in sheet resistance, consistent with their wider range of SSA values. It is clear from Fig. 7(a) that the sheet resistance decreases with increasing SSA regardless of EAF. The MCCE sheet resistance does indeed decrease with increasing EAF, but only because EAF for these conditions is proportional to SSA [see Fig. 6(a)]. However, for the RIE conditions, the sheet resistance actually increases with increasing EAF. While surface area increases with increasing RIE etch time, it is also accompanied with a

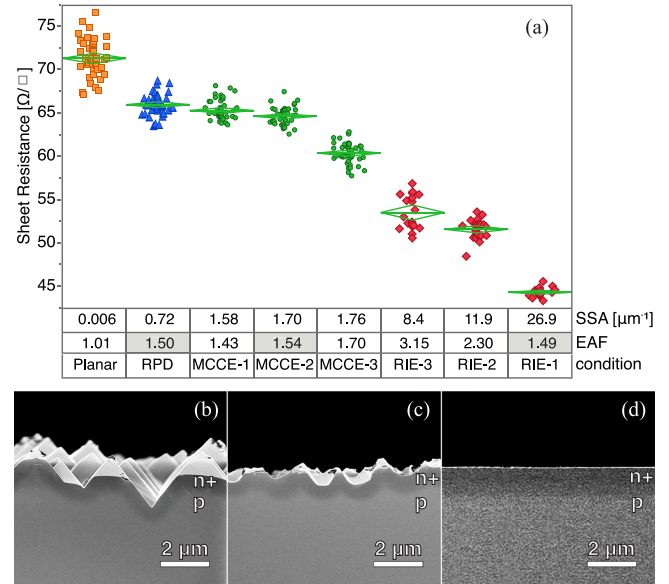


Fig. 7. (a) Post-diffusion sheet resistance for all texture conditions with SSA and EAF values indicated. Diamonds correspond to mean value 95% confidence intervals. Corresponding cross-sectional SEMDCI images for EAF ~ 1.5 conditions (b) RPD, (c) MCCE-2, and (d) RIE-1.

significant increase in texture volume, as is apparent in Figs. 4 and 5. This increase in texture volume results in decreasing SSA and increasing sheet resistance, which is consistent with reduced surface reactivity.

The corresponding cross-sectional SEMDCI images for the three conditions with similar EAF are shown in Fig. 7(b)–(d). For the RPD condition, shown in Fig. 7(b), the n^+ doping appears to be conformal with the textured surface while a large fraction of p-type (undiffused) area is observed within the texture layer. For the MCCE condition, shown in Fig. 7(c), the n^+ doping appears to be less conformal with the textured surface and exhibits a significantly lower fraction of p-type area within the texture layer compared with the RPD condition. The RIE-1 condition, shown in Fig. 7(d), exhibits a deeper junction and the n^+ region has a more uniform vertical distribution below the surface compared to the RPD and MCCE conditions, indicating fully doped texture features. These results indicate that despite having the same available surface area to react with PSG, the resulting sheet resistance for these three conditions is determined by their SSA.

C. 3-D Diffusion Simulations

In order to gain insight into the RIE B-Si sheet resistance trend, we simulated our diffusion process for two nanocone conditions, with dimensions based on AFM statistics. Fig. 8(a) shows the AFM height distributions for RIE-1 and RIE-3, with peak values of 28 and 352 nm, respectively. The inset shows the corresponding slant angle distributions with peak values of 62.5° and 70° . The dimensions of the nanocones used for simulations were calculated using these peak values with the resulting schematics shown (and presented on the same scale) in Fig. 8(b). These conditions give a small-to-large-cone EAF

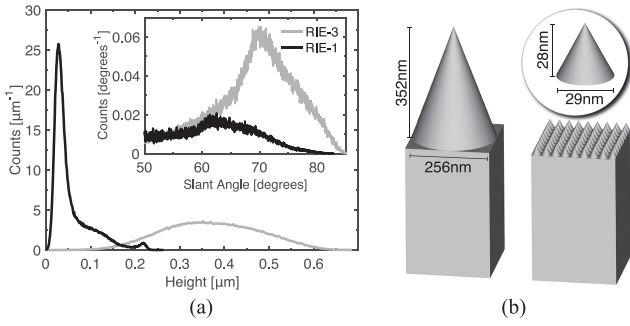


Fig. 8. (a) AFM height distributions for RIE-1 (black) and RIE-3 (gray). Inset: Corresponding slant angle distributions. (b) Schematics of nanocones (presented on the same scale and on the same sized cuboid substrates) with dimensions calculated using the peak values from (a). Inset: zoom-in of the smaller nanocone.

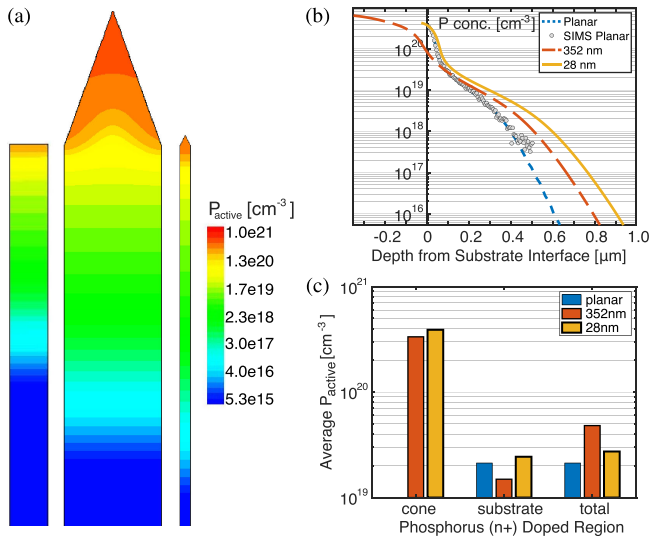


Fig. 9. 3-D simulation results. (a) P_{active} cross-sections for the planar condition (100 nm width) and two nanocone conditions with 352 and 28 nm heights, presented on the same dimensional scale. (b) Center P_{total} profile for the planar condition and its corresponding SIMS profile along with P_{active} line profiles for the two nanocones. (c) Volume average P_{active} values for the indicated n^+ regions of the 3-D unit-cells.

ratio of ~ 0.7 and a corresponding SSA ratio of ~ 9.3 (i.e., the larger nano-cone has a higher surface area, but lower SSA).

Fig. 9(a) shows the central cross-sections of the simulated active phosphorus concentration (P_{active}) for the planar condition (100 nm width) and the two nanocone conditions (352 and 28 nm heights), presented on the same dimensional scale. We will refer to the base of a cone as the substrate interface. It is clear from Fig. 9(a) that the larger nanocone exhibits higher doping at its tip, but significantly reduced doping towards its base, where radial doping is suppressed by the larger local volume. In fact, the P_{active} at its base is even lower than that at the surface of the planar condition. The smaller nanocone exhibits more uniform doping within its volume. Both nanocones exhibit significantly deeper doping into the substrate compared to the planar condition with the smaller nanocone exhibiting the

deepest metallurgical junction from the substrate interface (cone base).

The corresponding center-line profiles are shown in Fig. 9(b). The simulated total phosphorus concentration (P_{total}) profile for the planar condition shows good agreement with the measured SIMS profile. Fig. 9(b) also clearly shows the significant drop in doping towards the base of the larger nanocone, where its P_{active} equals that of the smaller nanocone at approximately its mid-height point. The trend of increasing metallurgical junction depth (from the substrate interface) with increasing SSA is also evident.

Fig. 9(c) shows the volume average P_{active} values for the following n^+ doped regions: within the cone, in the underlying substrate and for the total (from tip to junction), for all the 3-D unit cells. The average P_{active} is higher for the smaller nanocone condition in both its cone region and in the substrate. This result is consistent with its higher SSA leading to enhanced radial doping and enhanced substrate doping, as proposed in Section II-B. Fig. 9(c) also shows that the larger nanocone has the lowest substrate average P_{active} (even lower than planar) while its total average P_{active} is the highest. These results indicate that more P atoms are diffused by the larger (higher EAF) nanocone, but that the concentration is heavily skewed towards the tip. This offset was confirmed by calculating the total number of active P atoms per projected substrate area for the cone regions, which was 31 nm^{-2} for the 352 nm condition and 3 nm^{-2} for 28 nm condition. It is worth noting that the local SSA of the larger nanocone is significantly higher at its tip than its base, thus driving the local enhancement. It should also be noted that the inactive phosphorus concentrations, which impact recombination behavior [39], exhibited the same trends as those for the active concentrations shown in Fig. 9(c). However, gauging the impact of nanotexture morphology and SSA on recombination requires further simulation studies. We should also note that our approach of using the peak distribution values represents a first-order investigation. While the height distributions for RIE-1 and RIE-3, shown in Fig. 8(a), are significantly offset with limited overlap, the influence of such distributions on the global EAF and SSA, and their impact on doping, requires further study.

Local variations in average P_{active} also provide insight into a texture's sheet resistance, which is related to the lateral current flow within its n^+ regions. However, extended 3-D features will perturb this current. 3-D simulations of a random pyramid texture have shown negligible current at its tips attributed to their steep 55° slant angles [40]. The 70° slant-angled larger nanocone investigated here is therefore likely to have limited current flow at its tip. **As such we suspect that its highly doped tip would not significantly contribute to its sheet resistance.** It is more likely that **the current flow would be confined to the substrate and the lower part of its cone,** which have lower average P_{active} than the smaller nanocone. Such current flows would be consistent with the higher sheet resistance measured for RIE conditions with increasing size (higher EAF, lower SSA) shown in Fig. 7. However, simulating the current flow and total sheet resistance of 3-D B-Si textures requires further study and will be presented in future work.

D. Limitations and Caveats

AFM may not be suitable to extract SSA for other B-Si morphologies, including those with porous layers, or extremely high aspect ratio features. In such cases, other techniques may be needed to extract accurate SSA, like 3-D tomography approaches [41], [42] or N₂ adsorption-desorption isotherm measurements [43]. Despite possible measurement challenges, we suggest that SSA should be readily considered when studying B-Si properties, even if only as a relative/qualitative metric or estimated, for example from SEM analysis. We also note that the impact of diffusion process parameters on doping enhancement has not been addressed and requires further study.

V. CONCLUSION

In this article, we have demonstrated that B-Si's surface-to-volume ratio, or SSA, is a better indicator of reduced sheet resistance than surface area as it is directly related to surface reactivity. We showed that B-Si post-POCl₃ diffusion sheet resistance decreased with increasing SSA, regardless of surface area. In fact, for RIE B-Si textures with increasing aspect ratio, sheet resistance actually increased with increasing surface area due to the corresponding significant increase in texture volume and thus decrease in SSA. 2-D dopant contrast imaging of textures with similar surface areas but different volumes indicated that the extent of doping within features increases with increasing SSA. We also demonstrated via 3-D diffusion simulations of nanocones that a higher SSA feature, even with lower surface area, enhances radial doping within the feature and leads to a deeper metallurgical junction in the underlying substrate. The simulated 3-D distributions of active dopants were also consistent with the lower sheet resistance observed for higher SSA textures. In general, our findings indicate that as silicon texture features become more nano in scale, their increasing SSA leads to reduced sheet resistance. We suggest SSA should be considered more readily when investigating B-Si and may prove useful for understanding its other properties and effects, including enhanced recombination.

ACKNOWLEDGMENT

The authors would like to thank the facilities and the scientific and technical assistance of the Australian Microscopy & Microanalysis Research Facility at the Electron Microscope Unit, The University of New South Wales. They would like to thank Duc Huy Dao and Khanh Vy Le at the Solar Industrial Research Facility, The University of New South Wales, for assistance with sample processing. They would also like to thank Dr. Bill Bin Gong and Dr. Songyan Yin at the Surface Analysis Laboratory at the Solid State and Elemental Analysis Unit, The University of New South Wales, for the SIMS measurement. The responsibility for the views, information, or advice expressed herein is not accepted by the Australian Government. The RIE fabrication was supported by the Velux Foundation project nr. 13891 in Denmark.

REFERENCES

- [1] H. Foell, M. Christophersen, J. Carstensen, and G. Hasse, "Formation and application of porous silicon," *Mater. Sci. Eng. R Rep.*, vol. 39, pp. 93–141, 2002.
- [2] L. L. Ma *et al.*, "Wide-band 'black silicon' based on porous silicon," *Appl. Phys. Lett.*, vol. 88, no. 17, 2006, Art. no. 171907.
- [3] H. Jansen, M. de Boer, R. Legtenberg, and M. Elwenspoek, "The black silicon method: A universal method for determining the parameter setting of a fluorine-based reactive ion etcher in deep silicon trench etching with profile control," *J. Micromechan. Microeng.*, vol. 5, no. 2, pp. 115–120, 1995.
- [4] J. S. Yoo *et al.*, "Black silicon layer formation for application in solar cells," *Sol. Energy Mater. Sol. Cells*, vol. 90, no. 18, pp. 3085–3093, 2006.
- [5] Y.-F. Huang *et al.*, "Improved broadband and quasi-omnidirectional anti-reflection properties with biomimetic silicon nanostructures," *Nat. Nanotechnol.*, vol. 2, no. 12, pp. 770–774, 2007.
- [6] Z. Huang, N. Geyer, P. Werner, J. de Boor, and U. Gösele, "Metal-assisted chemical etching of silicon: A review," *Adv. Mater.*, vol. 23, no. 2, pp. 285–308, 2011.
- [7] K. Tsujino, M. Matsumura, and Y. Nishimoto, "Texturization of multicrystalline silicon wafers for solar cells by chemical treatment using metallic catalyst," *Sol. Energy Mater. Sol. Cells*, vol. 90, no. 1, pp. 100–110, 2006.
- [8] S. Bastide, N. L. Quang, R. Monna, and C. Lévy-Clément, "Chemical etching of Si by Ag nanocatalysts in HF-H₂O₂: Application to multicrystalline Si solar cell texturisation," *Phys. Status Solidi C*, vol. 6, no. 7, pp. 1536–1540, 2009.
- [9] S. Zou *et al.*, "Complementary etching behavior of alkali, metal-catalyzed chemical, and post-etching of multicrystalline silicon wafers," *Prog. Photovolt. Res. Appl.*, vol. 27, no. 6, pp. 511–519, 2019.
- [10] H. Lin *et al.*, "Developing controllable anisotropic wet etching to achieve silicon nanorods, nanopencils and nanocones for efficient photon trapping," *J. Mater. Chem. A*, vol. 1, no. 34, pp. 9942–9946, 2013.
- [11] X. Liang *et al.*, "Inverted silicon nanopencil array solar cells with enhanced contact structures," *Sci. Rep.*, vol. 6, no. 1, 2016, Art. no. 34139.
- [12] J. Chen *et al.*, "Fabrication of high-performance ordered radial junction silicon nanopencil solar cells by fine-tuning surface carrier recombination and structure morphology," *Nano Energy*, vol. 56, pp. 604–611, 2019.
- [13] F. Wu *et al.*, "Suppression of surface and auger recombination by formation and control of radial junction in silicon microwire solar cells," *Nano Energy*, vol. 58, pp. 817–824, 2019.
- [14] J. Sheng *et al.*, "MACE texture optimization for mass production of high-efficiency multi-crystalline cell and module," *IEEE J. Photovolt.*, vol. 9, no. 3, pp. 918–925, May 2019.
- [15] J. Oh, H.-C. Yuan, and H. M. Branz, "An 18.2%-efficient black-silicon solar cell achieved through control of carrier recombination in nanostructures," *Nat. Nanotechnol.*, vol. 7, no. 11, pp. 743–748, 2012.
- [16] X. Dai *et al.*, "The influence of surface structure on diffusion and passivation in multicrystalline silicon solar cells textured by metal assisted chemical etching (MACE) method," *Sol. Energy Mater. Sol. Cells*, vol. 186, pp. 42–49, 2018.
- [17] P. Li *et al.*, "Effective optimization of emitters and surface passivation for nanostructured silicon solar cells," *RSC Adv.*, vol. 6, no. 106, pp. 104073–104081, 2016.
- [18] T. H. Fung *et al.*, "Improved emitter performance of RIE black silicon through the application of in-situ oxidation during POCl₃ diffusion," *Sol. Energy Mater. Sol. Cells*, vol. 210, 2020, Art. no. 110480.
- [19] M. Otto *et al.*, "Extremely low surface recombination velocities in black silicon passivated by atomic layer deposition," *Appl. Phys. Lett.*, vol. 100, no. 19, 2012, Art. no. 191603.
- [20] P. Repo *et al.*, "Effective passivation of black silicon surfaces by atomic layer deposition," *IEEE J. Photovolt.*, vol. 3, no. 1, Jan. 2013, pp. 90–94.
- [21] B. Kafle *et al.*, "On the nature of emitter diffusion and screen-printing contact formation on nanostructured silicon surfaces," *IEEE J. Photovolt.*, vol. 7, no. 1, pp. 136–143, Jan. 2017.
- [22] T. P. Pasanen, H. S. Laine, V. Vähänissi, J. Schön, and H. Savin, "Black silicon significantly enhances phosphorus diffusion gettering," *Sci. Rep.*, vol. 8, no. 1, 2018, Art. no. 1991.
- [23] A. R. Stilling-Andersen, O. Solodovnikova, R. S. Davidsen, O. Hansen, and B. Iandolo, "Diffusion of phosphorous in black silicon," in *Proc. IEEE 7th World Conf. Photovolt. Energy Convers.*, 2018, pp. 2939–2942.
- [24] S. Zhong *et al.*, "Influence of the texturing structure on the properties of black silicon solar cell," *Sol. Energy Mater. Sol. Cells*, vol. 108, pp. 200–204, 2013.

- [25] B. Kafle *et al.*, “On the emitter formation in nanotextured silicon solar cells to achieve improved electrical performances,” *Sol. Energy Mater. Sol. Cells*, vol. 152, pp. 94–102, 2016.
- [26] K. Drabczyk, P. Panek, and M. Lipiński, “The influence of porous silicon on junction formation in silicon solar cells,” *Sol. Energy Mater. Sol. Cells*, vol. 76, no. 4, pp. 545–551, 2003.
- [27] G. Scardera, D. Poplavsky, M. Burrows, and S. Shah, “Methods of using a silicon nanoparticle fluid to control in situ a set of dopant diffusion profiles,” U.S. Patent 8,163,587, 2012.
- [28] Z. Shen *et al.*, “Black silicon on emitter diminishes the lateral electric field and enhances the blue response of a solar cell by optimizing depletion region uniformity,” *Scripta Mater.*, vol. 68, no. 3, pp. 199–202, 2013.
- [29] A. N. Goldstein, “The melting of silicon nanocrystals: Submicron thin-film structures derived from nanocrystal precursors,” *Appl. Phys. A*, vol. 62, no. 1, pp. 33–37, 1996.
- [30] P. Klapetek, D. Necas, and C. Anderson, “Gwyddion user guide 2012,” Accessed: Sep. 26, 2019. [Online]. Available: <http://gwyddion.net/documentation/user-guide-en>
- [31] D. Shir, B. Z. Liu, A. M. Mohammad, K. K. Lew, and S. E. Mohny, “Oxidation of silicon nanowires,” *J. Vac. Sci. Technol. B Microelectron. Nanometer Struct. Process.*, vol. 24, no. 3, pp. 1333–1336, 2006.
- [32] A. Bentzen, “Phosphorus diffusion and gettering in silicon solar cells,” Ph.D., Dept. Phys., Univ. Oslo, Oslo, Norway, 2006.
- [33] P. Menna, G. Di Francia, and V. L. Ferrara, “Porous silicon in solar cells: A review and a description of its application as an AR coating,” *Sol. Energy Mater. Sol. Cells*, vol. 37, no. 1, pp. 13–24, 1995.
- [34] N. David and K. Petr, “Gwyddion: An open-source software for SPM data analysis,” (in English), *Open Phys.*, vol. 10, no. 1, pp. 181–188, 2012.
- [35] D. Payne *et al.*, “Understanding the optics of industrial black silicon,” *AIP Conf. Proc.*, vol. 1999, no. 1, 2018, Art. no. 050007.
- [36] S. L. Elliott, R. F. Broom, and C. J. Humphreys, “Dopant profiling with the scanning electron microscope—A study of Si,” *J. Appl. Phys.*, vol. 91, no. 11, pp. 9116–9122, 2002.
- [37] D. Venables, H. Jain, and D. C. Collins, “Secondary electron imaging as a two-dimensional dopant profiling technique: Review and update,” *J. Vac. Sci. Technol. B Microelectron. Nanometer Struct. Process., Meas., Phenomena*, vol. 16, no. 1, pp. 362–366, 1998.
- [38] S. P. U. Guide, Mountain View, CA, USA: Synopsys, 2011.
- [39] B. Min *et al.*, “Heavily doped Si:P emitters of crystalline Si solar cells: Recombination due to phosphorus precipitation,” *Phys. Status Solidi–Rapid Res. Lett.*, vol. 8, no. 8, pp. 680–684, 2014.
- [40] V. Moroz, J. Huang, G. Letay, and I. Martin-Bragado, “Modeling and optimization of solar cells,” *AIP Conf. Proc.*, vol. 1496, no. 1, pp. 201–205, 2012.
- [41] Y. Zhang *et al.*, “Advanced characterisation of black silicon surface topography with 3D PFIB-SEM,” in *Proc. IEEE 46th Photovolt. Specialists Conf.*, 2019, pp. 0825–0828.
- [42] Y. Zhang *et al.*, “3D characterisation using plasma FIB-SEM: A large-area tomography technique for complex surfaces like black silicon,” *Ultramicroscopy*, vol. 218, 2020, Art. no. 113084.
- [43] R. M. Tiggelaar, V. Verdoodt, H. Eghbali, G. Desmet, and J. G. E. Gardeniers, “Characterization of porous silicon integrated in liquid chromatography chips,” *Lab Chip*, vol. 9, no. 3, pp. 456–463, 2009.